FULL PAPER

Organic Phototransistors

ADVANCED
OPTICAL
MATERIALS

www.advopticalmat.de

Flexible and Transparent Organic Phototransistors on Biodegradable Cellulose Nanofibrillated Fiber Substrates

Junsu Park, Jung-Hun Seo, Seung-Won Yeom, Chunhua Yao, Vina W. Yang, Zhiyong Cai, Young Min Jhon,* and Byeong-Kwon Ju*

This work demonstrates flexible, transparent phototransistors that can detect visible light with nontoxic organic active materials on biodegradable substrates toward environment-friendly electronics. The molybdenum trioxide (MoO_3)-buffered indium zinc oxide as high-performance hole injector and transparent electrodes is applied for the first time to organic phototransistors on cellulose nanofibrillated fiber substrates to achieve more than 70% of transmittance in the visible range (400–750 nm) while showing high conductivity under multiple bendings. Excellent electrical switching characteristics are obtained from transistors using a pentacene active layer with a saturation mobility value of 1.40 cm^2 V^{-1} s^{-1}. The phototransistors, which can detect visible light and perform in two operation modes, exhibit a maximum responsivity of 54.8 A W^{-1} and a photosensitivity of 24.4 under white light illumination at an intensity of 0.12 mW cm^{-2}. Moreover, the devices show a stable operation during mechanical bending tests with radii ranging from 100 to 5 mm and cyclic bending tests of up to 2000 cycles at a fixed radius of 5 mm. The results suggest that these flexible phototransistors with properties of transparency and biodegradability have considerable potential for use in low-cost and eco-friendly disposable sensor systems.

1. Introduction

In the era of the Internet of things, the high-performance flexible photodetector is one of the key elements that enable to monitor or sense various environmental conditions. In particular, as the more flexible electronic applications are used in attachable or implantable bioelectronics, health care, and environment monitoring system, there is an increased demand for high-performance flexible photodetectors that possess nontoxicity, good transparency, and biodegradability, simultaneously.[1,2] At the same time, reducing the amount of working electronic waste is ecologically critical to protect the environment and conserve the finite natural resources.[3–5]

Although the advent of biodegradable cellulose nanofibrillated fiber (CNF) substrate enables us to realize fully or partially biodegradable electronic applications,[6–8] as of yet, none of the aforementioned needs and issues have been realized together. For example, Lamprecht et al. reported flexible organic photodetector on cellulose paper substrate,[9] but CuPc that was used in the active layer is known to be toxic to human or environment.[10] In fact, some of the widely used organic semiconductors such as CuPc and C_{60} contain a significant amount of hazardous elements.[11,12] Some of the translational electronics that were initiated by Rogers' group performed excellent biocompatibility and degradability, but most of the devices were not transparent due to the use of magnesium electrodes;[13–15] thus, it limits the use in some specific biomedical area or environmental applications that require high transparency such as in vivo neural imaging and optogenetic applications.[16,17]

In this study, we realize the highly sensitive flexible organic phototransistors (OPTs) that fulfill nontoxicity, transparency, and biodegradability by employing various functional materials. First, pentacene was chosen as a nontoxic organic semiconductor that serves as an active layer of the phototransistor.[18,19] The combination of nontoxic active material and biodegradable film (CNF substrate) as the alternative substrate offers to demonstrate eco-friendly electronics that help reduce the accumulation of dangerous electronic wastes and solve environmental problems. Second, molybdenum trioxide (MoO_3)-buffered

J. Park, Dr. S.-W. Yeom, Prof. B.-K. Ju
Display and Nanosystem Laboratory
College of Engineering
Korea University
Anam-dong, Seoul 02841, Republic of Korea
E-mail: bkju@korea.ac.kr

J. Park, Dr. Y. M. Jhon
Sensor System Research Center
Korea Institute of Science and Technology
Seoul 02792, Republic of Korea
E-mail: ymjhon@kist.re.kr

Prof. J.-H. Seo
Department of Materials Design and Innovation
University at Buffalo
The State University of New York
Buffalo, NY 14260, USA

Dr. C. Yao
Department of Material Sciences and Engineering
University of Wisconsin–Madison
Madison, WI 53706, USA

V. W. Yang, Dr. Z. Cai
Forest Products Laboratory
USDA Forest Service
Madison, WI 53726, USA

**ADVANCED
SCIENCE NEWS**

www.advancedsciencenews.com

**ADVANCED
OPTICAL
MATERIALS**

www.advopticalmat.de

Figure 1. a) Bottom-gate/top-contact OPT device structure on a CNF substrate. b) A photograph of the OPTs above the DIANA Lab logo. c) Optical transmittance spectra of the CNF substrate and of the devices on CNF substrates with IZO and Au S/D electrodes.

transparent indium zinc oxide (IZO) electrode was employed not only to obtain a high transparency at a visible wavelength but also to improve the contact resistance. The phototransistors with a MoO_3 buffer layer exhibit excellent electrical characteristics that are comparable to those of devices with metal electrodes. In addition, the phototransistors can detect visible light and can operate in both a photovoltaic mode and a photocurrent mode that offer more flexibility depending on the type of applications. Over 2000 times of mechanical bending test confirms stable and reliable electrical performance. Overall, high-performance flexible OPTs that are combined with eco-friendly materials and the transparent electrode will open up new avenues for flexible photosensors toward future medical and environment monitoring applications.

2. Results and Discussion

Figure 1a presents a schematic illustration of the flexible OPT device on a CNF substrate. As mentioned above, IZO was used for gate and source/drain electrodes due to its high transparency and low-temperature process. The room temperature fabrication process is desirable to minimize thermal damage of the organic semiconductor and CNF film. The average sheet resistance of the 200 nm thick IZO electrode was measured to be 37.5 Ω sq^{-1}, which is a slightly higher contact resistance than that of metal electrodes. Such a large sheet resistance of the IZO electrode is mostly attributed to the formation of a large hole-injection barrier between the IZO electrode and the pentacene layer that was created by thermal damage. Thus, transition metal oxide (TMO)-based buffer layers, such as MoO_3, vanadium oxide (V_2O_5), and Tungsten trioxide (WO_3), have been inserted to lower the hole-injection barrier.[20,21] Among various TMO-based materials, MoO_3 was chosen as a hole-injection barrier between IZO and pentacene, because organic devices with a MoO_3 buffer layer showed a good optical transparency in the visible light region and improved electrical characteristics.[21,22] The pentacene active layer, which exhibits a high carrier mobility because of its crystal structure and the considerable overlap of the frontier molecular orbitals,[23,24] was deposited using thermal evaporation. In the bottom-gate/top-contact structure, for high performance, the crystalline quality of pentacene is largely determined by the roughness of the dielectric layer. The spin-coated polymethyl methacrylate (PMMA) layer, which serves as the gate dielectric layer of the devices, not only offers moderate dielectric properties with a high surface gloss and high transparency but also reduces the surface roughness of the IZO gate electrode on the CNF film (Figure 3).

Additionally, matching the surface free energy between PMMA and pentacene allows us to realize high-performance transistors.[25] PMMA is thus suitable as a dielectric layer for pentacene-based OPTs with bottom-gate/top-contact structures. Figure 1b is a digital camera image of the optically transparent devices, which consist of a 3 × 2 transistor array on a CNF substrate. The high optical transparency of the OPTs can be attributed to the transparent IZO electrodes with the MoO_3 buffer layer and the PMMA dielectric layer. The transmittance spectrum of the transistor with IZO electrodes is shown in Figure 1c, along with spectra of the CNF substrate. The transmittance of a transistor with 80 nm thick Au as the source/drain electrodes was also measured for comparison. Au is most commonly used in the source/drain electrodes of pentacene-based organic thin-film transistors (OTFTs) because the energy barrier at the interface between the semiconductors and Au electrodes creates a favorable hole injection.[26,27] The average transmittance of the six layers (CNF/IZO/PMMA/pentacene/MoO_3/IZO) was 70.4% in the visible range (400–750 nm). When changing the source/drain electrode to 80 nm thick Au, an average transmittance of 42.1% was observed in the visible range. Evidently, IZO is more suitable than Au as the electrode of transistors for transparent electronics when considering the difference between the transmittance of these two devices (around 28%).

The hole-injection barrier height at the IZO–pentacene interfaces with and without the TMO buffer layer was measured using ultraviolet photoelectron spectroscopy (UPS) to calculate the work function of each material and the highest occupied molecular orbital (HOMO) onset of pentacene on IZO, as shown in **Figure 2**a. The measured hole-injection barrier between IZO and pentacene without the TMO buffer is 0.65 eV, while the HOMO onset of pentacene on MoO_3/IZO is 0.42 eV, which is about 35% less than that of directly deposited pentacene on IZO. The energy-level diagrams created using UPS spectra taken at the IZO/MoO_3/pentacene interface are shown in Figure 2b. The HOMO onset of pentacene on MoO_3/IZO is 0.42 eV, which is less than that of directly deposited pentacene on IZO. In addition to lowering the hole-injection barrier height, we found that electron transfer is favorable across the MoO_3/pentacene junction because of the well-aligned conduction band edge of MoO_3 and the HOMO of pentacene.[21] Therefore, the deposition of the MoO_3 buffer layer between IZO and pentacene facilitates charge carrier transport into the pentacene layer by the charge transfer mechanism.

The growth and morphology of the pentacene semiconductor layer, which are highly related to the charge-carrier mobility of OTFTs, are affected by the surface state of the dielectric layer
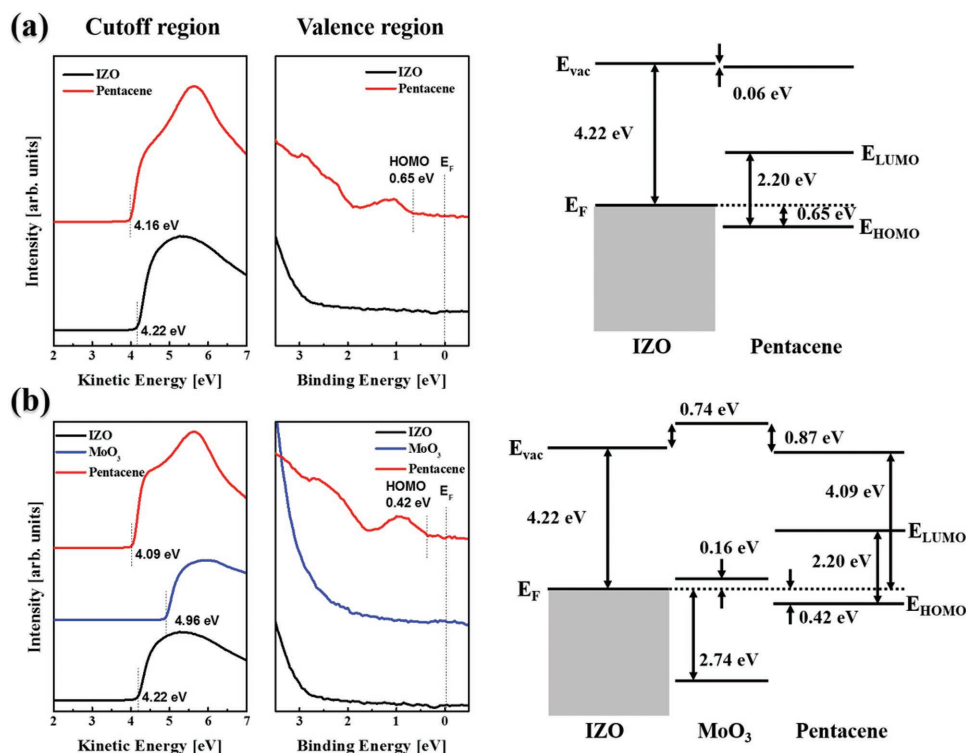
**ADVANCED
SCIENCE NEWS**

www.advancedsciencenews.com

**ADVANCED
OPTICAL
MATERIALS**

www.advopticalmat.de

Figure 2. A schematic energy level diagram based on the measured ultraviolet photoelectron spectroscopy (UPS) spectra in the normalized secondary cutoff region and the valence region taken from a) the IZO thin film and pentacene on IZO, and b) IZO, MoO_3/IZO, and pentacene/MoO_3/IZO.

in the bottom-gate structure.[23] **Figure 3**a–d shows atomic force microscopy (AFM) topographic images of four samples, including a CNF substrate, IZO on CNF, PMMA/IZO on CNF, and pentacene/PMMA/IZO on CNF. Considering the roughness of a few nanometers of well-known flexible substrates such as polyethersulfone or polyethylene terephthalate substrate, the

CNF substrate has a relatively rough surface (a root mean square (rms) roughness (R_{rms}) of 19.8 nm and a peak-to-valley roughness (R_{pv}) of 129.9 nm) due to the randomly distributed nanofibrils. As shown in Figure 3b, the deposition of the IZO layer as a gate electrode slightly decreases the R_{rms} of the CNF film to 16.1 nm and the R_{pv} to 122.6 nm. This reveals that the IZO
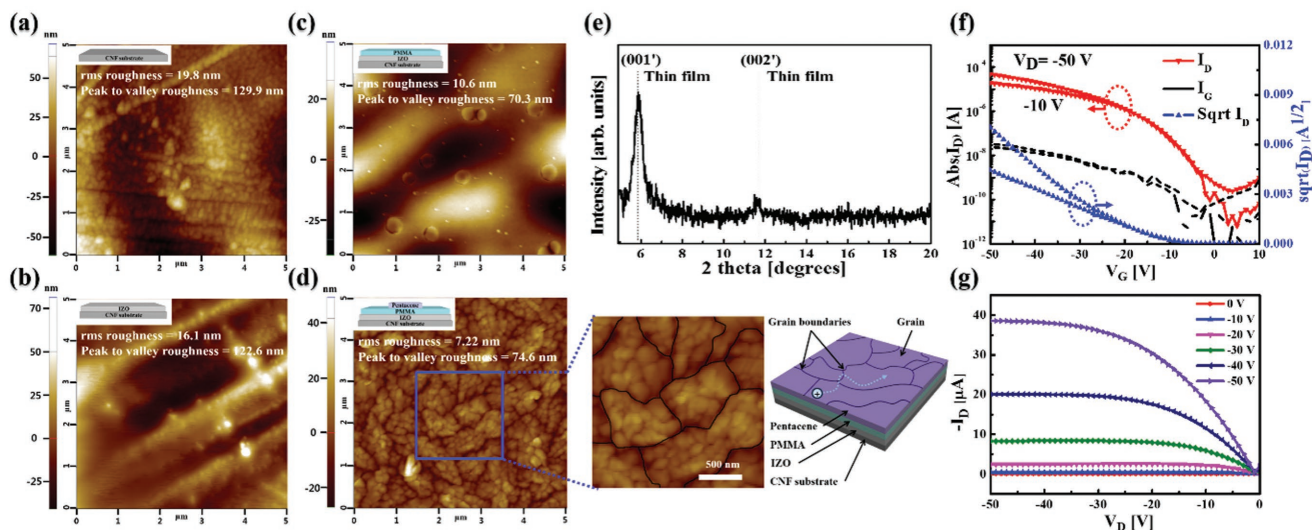

Figure 3. AFM topographic images of a) the CNF substrate, b) IZO/CNF substrate, and c) PMMA/IZO/CNF substrate. d) AFM image and schematic diagram of pentacene on the PMMA/IZO/CNF substrate with the grain and grain boundaries. e) XRD spectrum of the pentacene thin films on the PMMA/IZO/CNF substrate. f) Transfer (I_D vs V_G) with I_D (red), square root of I_D (blue), gate leakage current I_G (black), and g) output (I_D vs V_D) characteristics with different V_G values ranging from 0 to −50 V with a −10 V step of OPTs using IZO electrodes with the MoO_3 buffer layer on the CNF substrate.

ADVANCED
SCIENCE NEWS
www.advancedsciencenews.com

ADVANCED
OPTICAL
MATERIALS
www.advopticalmat.de

layer is insufficient for uniformly smoothing the surface of CNF substrate. On the other hand, the surface morphology can be further improved by using PMMA as a dielectric layer, resulting in an R_{rms} of 10.6 nm (Figure 3c). This also significantly reduces the R_{pv} to 70.3 nm, indicating that the PMMA layer uniformly covers the surface of the IZO on CNF. We believe that the dramatic reduction of R_{pv} can be attributed to the deposition of the PMMA layer by spin-coating in the solution process. The grain size and crystalline qualities of the 70 nm thick pentacene film on the PMMA/IZO/CNF substrate were observed as shown in Figure 3d. The polycrystalline pentacene film is formed with an average grain size of 950 nm; the grain boundaries determine the charge transport inside the pentacene layers by scattering the carriers, which lowers the mobility.[28] X-ray diffraction (XRD) was performed to analyze the crystalline quality of the pentacene thin film on PMMA/IZO on the CNF substrate. As shown in Figure 3e, we can only observe the (00l') diffraction peak, attributed to the "thin-film phase," with an interlayer spacing of 15.4 Å.[25] This reveals that pentacene crystallizes with a herringbone arrangement and forms a fiber structure with the a–b plane oriented parallel to the substrate.[23,24] The AFM images and XRD spectra indicate that the pentacene films were deposited with a polycrystalline structure due to the improved roughness of the CNF films by the spin-coated PMMA layers. Figure 3f,g presents the transfer (drain current I_D vs gate voltage V_G) and output (I_D vs drain voltage V_D) characteristics, respectively, of transistors using IZO electrodes with MoO$_3$ buffer layer. The devices have a 2500 µm channel width, 100 µm length, and 6.20 nF cm^{-2} capacitance per unit area of the gate insulator. The drain–source on-current scales linearly with the increase in channel width-to-length ratio (Figure S1, Supporting Information), and the trend is very similar to that of previously reported pentacene-based OTFTs.[29] The fundamental OTFT parameters of these devices in the saturation regime ($V_G - V_T < V_D$) are obtained from the following equation

$$I_D = \frac{W}{2L} \mu_{sat} C_i \left(V_G - V_T \right)^2 \qquad (1)$$

where I_D is the source-to-drain current; W and L are the width and length of the channel, respectively; μ_{sat} is the saturation mobility; C_i is the capacitance per unit area of the gate insulator; V_G is the gate voltage; and V_D is the drain voltage. V_T was evaluated from the x-axis intercept of the plot of versus V_G. The subthreshold swing (SS) is determined from the following equation

$$S = \frac{dV_G}{d\left(\log I_D \right)} \qquad (2)$$

The electrical characteristics are $\mu_{sat} = 1.40 \ (\pm 0.213)$ cm^2 V^{-1} s^{-1}, $V_T = -13.8 \ (\pm 1.12)$ V, SS $= -4.54 \ (\pm 1.13)$ V decade^{-1}, and $I_{on}/I_{off} \approx 10^5$ at $V_D = -50$ V. In comparison to the operation of devices with IZO electrodes without a MoO$_3$ layer, the OPTs exhibited high performance (Figure S2a, Supporting Information). This improvement in electrical characteristics is attributed to the lowering of the hole-injection barrier and the charge transfer mechanism between MoO$_3$ and organic material as described above. When comparing the thin-film transistor characteristics

with those of devices using Au electrodes, thin-film transistors (TFTs) using IZO with MoO$_3$ exhibit comparable performance (Figure S2b, Supporting Information). The parameters of the TFTs with different source/drain electrode materials (IZO with MoO$_3$, only IZO, and Au) are listed in Table S1 in the Supporting Information. Kang et al. reported a pentacene-based organic transistor that has an organic heterointerface between a small-molecule dielectric and pentacene on a Si wafer.[30] This device exhibited a higher hole mobility (up to 6.3 cm^2 V^{-1} s^{-1}) than our device with fewer grain boundaries. However, this method requires atomically smooth surface such as Si wafer to define a delicate organic heterointerface, thus it is not possible to apply to flexible electronics with rough flexible substrate such as CNF substrate. On the other hand, we have proved a comparable device performance with superior mechanical stability and durability by the mechanical bending test and cyclic bending test as shown in Figure 8.

Figure 4a presents a cross-sectional view of the phototransistor under white light illumination from above using a Xenon arc lamp. In Figure 4b, the transfer characteristics are shown at $V_D = -50$ V in the dark and under light illumination at light intensities of 0.12, 0.36, 0.6, 0.84, and 1.2 mW cm^{-2}. The photo-to-dark current ratio (I_{ph}/I_{dark}) of the OPTs increases with the increase in light intensity by up to 10^2 times under light of 1.2 mW cm^{-2} at $V_G = 0$ V. This indicates that the current can be controlled by the absorption of light for OPTs without the field effect by the gate electrode. V_T shifted toward more positive values when the incident optical power increased. The positive shifting in V_T is responsible for light absorption in the channel regions, which generates charge carriers. It should be noted that the generation of charge carriers by light illumination in MoO$_3$-buffered IZO electrodes is negligible compared with that in the pentacene active layer, because IZO of the heavily doped degenerate semiconductor and MoO$_3$ of TMO have a large band gap. These photoinduced holes and electrons easily move to the drain electrode and the source electrode, respectively, which leads to a positive shift of V_T and increase in I_D by lowering the hole-injection barrier for a p-channel OPT (Figure 4c).[11,31] Figure 4d shows the output characteristics at $V_G = -50$ V (on state) in the dark and under white light irradiation at different light intensities. The drain current in both the linear regime and saturation regime increases with increasing light intensity. The OPTs show that the maximum drain current increases by up to 42.5 µA at $V_D = -50$ V.

Photoresponsivity and photosensitivity are the two main factors that determine the performance of OPTs. The responsivity (R_{ph}), which reflects how much optical power is converted into electrical current, can be calculated from the following equation

$$R_{ph} = \frac{I_{ph}}{P_{opt}} = \frac{I_{D,ph} - I_{D,dark}}{P_{inc} A} \qquad (3)$$

where I_{ph} is the photocurrent, P_{opt} is the power of the incident light, P_{inc} is the light incident power per unit area, A is the area of the active region, and $I_{D,ph}$ and $I_{D,dark}$ are the drain currents under illumination and in the dark, respectively. The photosensitivity (P) is defined as the signal-to-noise ratio given by the following equation
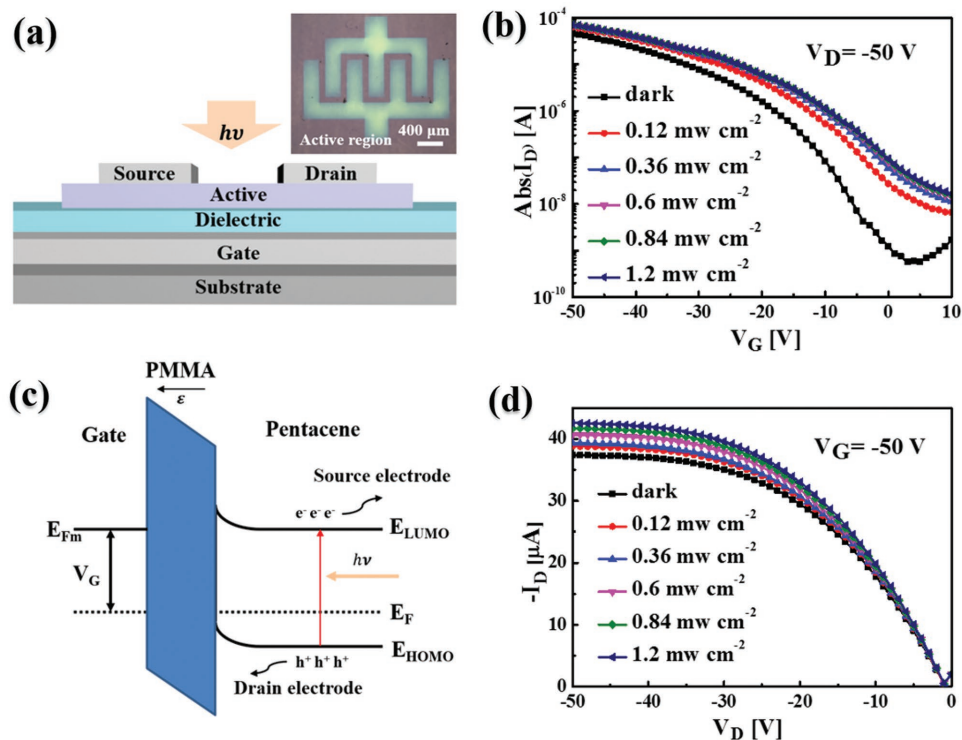
Figure 4. a) Device structure of the organic phototransistors on a CNF substrate with light illumination. The inset shows a microscopic image of the active region. b) Transfer (at $V_D = -50$ V) and d) output (at $V_G = -50$ V) characteristics in the dark and under light illumination at different light intensities. c) Energy band diagram of the organic phototransistors in the direction from the gate to the S/D electrodes when devices are under illumination with a negative gate bias.

$$P = \frac{\text{signal}}{\text{noise}} = \frac{I_{ph}}{I_{dark}} = \frac{I_{D,ph} - I_{D,dark}}{I_{D,dark}} \qquad (4)$$

Figure 5a shows the R_{ph} and P values of the OPTs under white light illumination at an intensity of 0.12 mW cm^{-2}; these values are given for different light intensities (Figure S3, Supporting Information). The highest value of R_{ph} was ≈ 54.8 A W^{-1} in the on state ($V_G = 50$ V), while the highest value of P was ≈ 24.4 in the off state ($V_G = 1$ V) under an intensity of 0.12 mW cm^{-2}. With increasing light intensity, R_{ph} decreases from 54.8 to 8.4 A W^{-1}, and P increases from 24.4 to 81.6, as shown in Figure 5b,c. Note that the decrease in R_{ph} is nonlinear, decreasing rapidly at low intensities but decreasing more gradually at high levels. The increase in P is similar to the change in R_{ph} at different light intensities. This may be due to increased carrier recombination with increasing light intensity.[32] As expected from Figure 4d, the highest value of R_{ph} in the linear regime ($V_D = -10$ V, $V_G = -50$ V) decreases from 13.8 to 1.8 A W^{-1} with increasing light intensity, as shown in Figure S4 in the Supporting Information. The trend of the responsivity with respect to the light intensity is very similar to the result in the saturation regime. The responsivity as a function of the optical power increases in proportion to the biased drain voltage. The demonstration of the operation of the phototransistor with different V_D biases indicates that the device can be operated in the linear regime and the saturation regime. As shown in Figure 5d, the phototransistor can be operated in two different modes: the first is the photovoltaic mode in the

turned-on state ($V_G \gg V_T$), and the second is the photoconductive mode in the turned-off state ($V_G < V_T$). In the first mode, the photocurrent can be expressed as[11]

$$I_{ph} = g_m \Delta V_T = \frac{AkT}{q} \ln\left(1 + \frac{\eta q \lambda P_{opt}}{I_{pd} hc}\right) \qquad (5)$$

where η is the quantum efficiency, P_{opt} is the incident optical power, I_{pd} is the dark current for minority charges, hc/λ is the photon energy, g_m is the transconductance, ΔV_T is the threshold voltage shift, and A is the fitting parameter. In the second mode, the photocurrent caused by a photoconductive effect can be modeled according to the following equation[11]

$$I_{ph,pc} = (q\mu_p pE)WD = BP_{opt} \qquad (6)$$

where μ_p is the hole mobility, p is the hole concentration, E is the electrical field in the channel, W is the gate width, D is the depth of the absorption region, and B is the fitting parameter. I_{ph} values are plotted as a function of incident optical powers in the turned-on state ($V_G = -50$ V and $V_D = -50$ V) and turned-off state (V_G was extracted at the minimum I_D, and $V_D = -50$ V). The closed-square and open-square symbols denote the experimental data points, and the dotted lines show results fitted using Equations (5) and (6). The well-fitted results indicate that our phototransistor operates not only in a photovoltaic mode in the turned-on state but also in a photocurrent mode in the turned-off state; this agrees well with previous OPTs.[11,33]
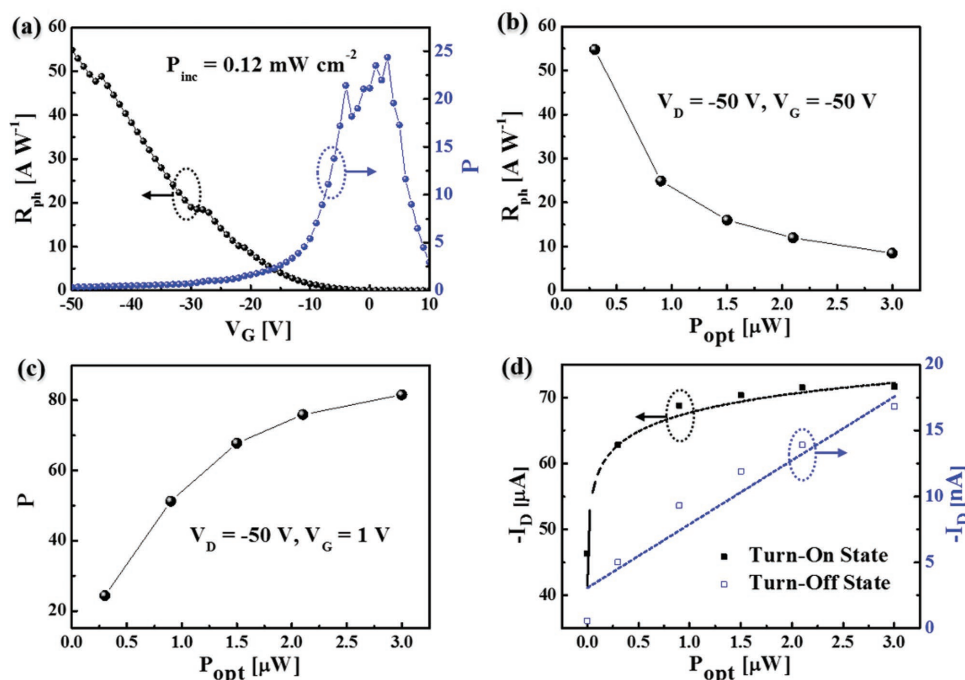
Figure 5. a) Responsivity and photosensitivity of OPTs as a function of V_G under white light illumination at an intensity of 0.12 mW cm^{-2}. b) Responsivity at fixed $V_D = -50$ V and $V_G = -50$ V and c) photosensitivity at fixed $V_D = -50$ V and $V_G = 1$ V as a function of the optical power. d) Photocurrent according to light power in turned-on ($V_G = -50$ V) and turned-off (minimum I_D) states at $V_D = -50$ V. The symbols are experimental data, while dotted lines indicate the fitted results using Equations (5) and (6).

The light-sensing characteristics with respect to visible light were also measured using the OPTs to investigate the effect on the photocurrent under different wavelengths. **Figure 6**a

shows the absorption spectrum of a 70 nm pentacene film on a PMMA/IZO/CNF substrate in the visible wavelength range (400–700 nm). The transfer characteristics of the device using
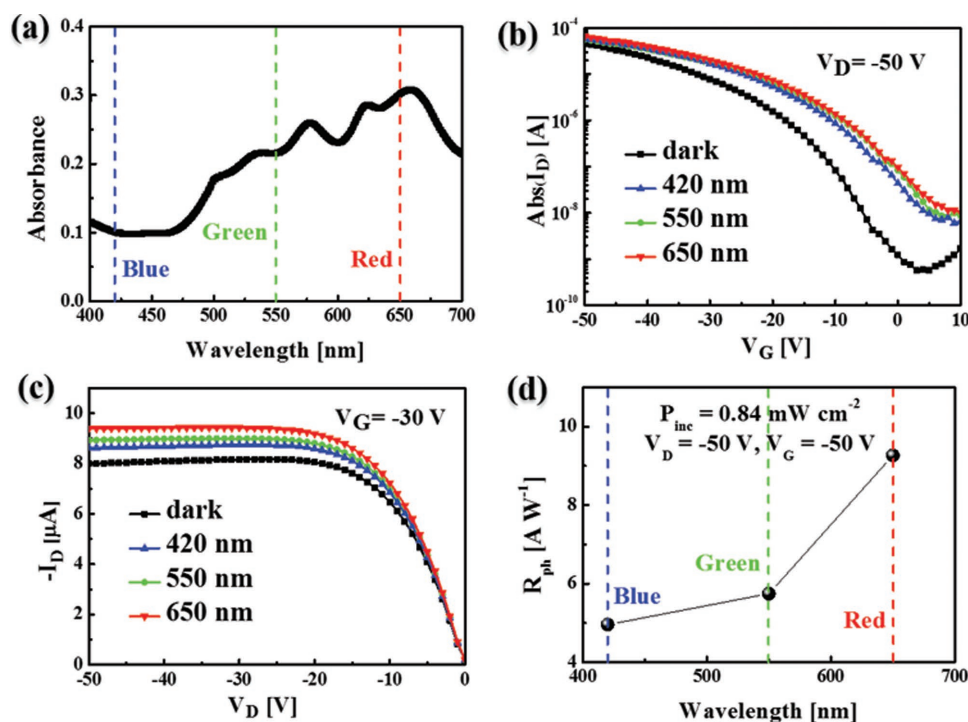

Figure 6. a) The absorption spectrum of the pentacene film in the visible wavelength range (400–700 nm). b) Transfer and c) output characteristics under dark and light illumination with various wavelengths (red, green, and blue). d) Responsivity as a function of wavelength.
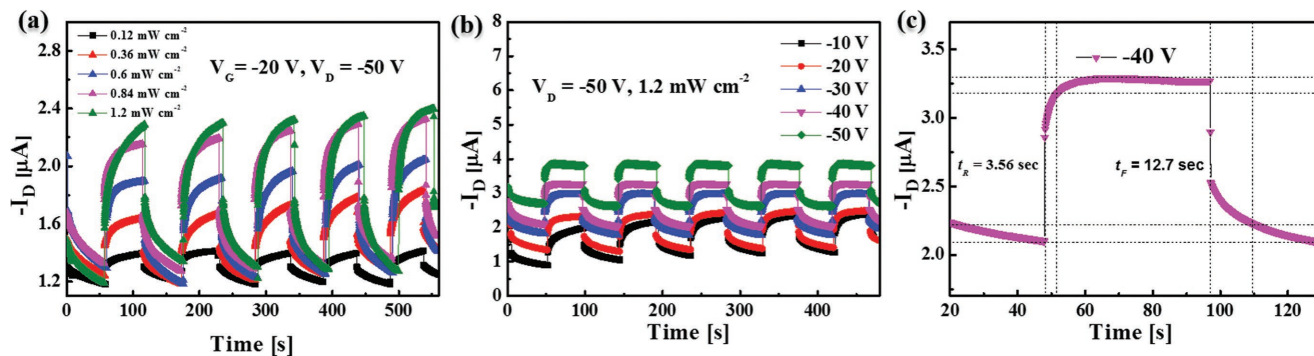
**ADVANCED
SCIENCE NEWS**
www.advancedsciencenews.com

**ADVANCED
OPTICAL
MATERIALS**
www.advopticalmat.de

Figure 7. Photoresponse (I_D vs time) characteristics of OPTs at a) $V_G = -20$ V and $V_D = -50$ V with various light intensities, and b) $V_D = -50$ V and $P_{inc} = 1.2$ mW cm^{-2} with different V_G. c) Enlarged single response time for turned-on (t_R) and turned-off (t_F) states from (b) at −40 V.

different wavelength filters (420 nm (blue), 550 nm (green), and 650 nm (red)) with the same power intensity of 0.84 mW cm^{-2} are shown in Figure 6b. Note that the illuminated light intensity with filters was limited to fixed values; however, we expect the OPT devices to exhibit similar results with different light intensities. The increased I_D and the positive shift of V_T under light exposure show the wavelength dependence: the device shows the highest photo-to-dark current under red-light illumination and the lowest value under blue-light illumination. These results are also evident in the output characteristics as shown in Figure 6c. The responsivities as a function of wavelength are shown in Figure 6d. The maximum responsivity at a voltage bias of $V_G = -50$ V and $V_D = -50$ V under red, green, and blue light illumination for the OPTs is calculated to be 9.27, 5.75, and 4.96 A W^{-1}, respectively. Therefore, with a larger absorbance, the device, which can detect the visible light, shows higher responsivity.

The drain currents as a function of time are shown in **Figure 7**. Figure 7a presents the time-resolved response of the OPTs upon white light illumination with different optical intensities at a fixed voltage bias of $V_G = -20$ V and $V_D = -50$ V. It can be clearly seen that light pulses cause the devices to switch between on and off states with the reproducibility and photoinduced I_D increasing proportionally to light intensity. The photoresponse under different gate bias voltages was also determined at $V_D = -50$ V and $P_{inc} = 1.2$ mW cm^{-2} as shown in Figure 7b. It was observed that both the dark current and the photocurrent increase with increasing gate bias voltage owing to the field effect and that OPTs show switching characteristics in response to the light being on/off, independent of the applied gate bias. The photoresponse of the device can thus be tuned by controlling the light intensity and applying an appropriate bias voltage. A single cycle of photoresponse under light illumination is plotted in Figure 7c to observe the rise time (t_R, time for the photocurrent to rise from 10% to 90%) and the fall time (t_F, time for the photocurrent to decrease from 90% to 10%). The device's rise and fall times of 3.56 and 12.7 s, respectively, are related to carrier recombination, generation, and the minority carrier life time. Compared with the response times during light activation, when the light is off, the relatively slow deactivation response, which exhibits exponential decay, might be attributed to the recombination behavior of the photogenerated carriers in the active region. We believe that the response time

can be further improved by optimizing the device design, including the semiconductor material, aligned gate electrodes, and channel lengths. In recent years, there have been many attempts to research pentacene-based OPT devices with Au electrodes for detecting visible light, showing less than 3 A W^{-1} of the photoresponsivity and switching characteristics in response to turning the light on/off.[34,35] Our pentacene-based devices with transparent electrodes exhibit a larger photoresponsivity (up to 54.8 A W^{-1}), which is similar to that of single crystalline semiconductor based flexible phototransistor[36] and faster response time than other reported organic phototransistors.

The mechanical bending effects on the characteristics of the flexible transistor were characterized to investigate flexibility and durability of both OPTs and CNF substrate. For the test, the device was attached to metal bending substrates with radii varying from 100 to 5 mm. An optical image of the flexible transistor under the bending tensile condition with a radius of 100 mm is shown in **Figure 8**a. The transfer characteristics of the OPTs at $V_D = -50$ V exhibited stable operation as a function of the applied tensile strains ranging from 0.05% to 0.99% as shown in Figure 8b. The tensile strain was calculated as; strain (%) = $1/[(2R/\Delta R)] + 1] \times 100$, where R is the fixture radius and ΔR is the thickness of the bent object containing the CNF substrate (100 μm), IZO gate electrode (200 nm), PMMA dielectric (500 nm), pentacene semiconductor (70 nm), and IZO source/drain electrodes with MoO$_3$ (220 nm). Figure 8c shows the variation of μ_{sat} and the on and off current of the flexible OPTs as a function of the applied tensile strains. Although the measured μ_{sat} decreased as the strain increased, which may be due to the increase in the spacing of molecules and crystal domains,[37] it still remained above 1.17 cm^2 V^{-1} s^{-1} under a strain of 0.99%. Moreover, a stable on/off ratio of 10^5 was achieved under strain, showing that mechanical bending did not significantly affect the electrical properties. A cyclic bending test of the transistors was also performed for 2000 cycles at a fixed bending radius of 5 mm with the curvature calculated as illustrated in Figure 8d. As shown in Figure 8e, the shift of the drain current in the transfer curves at $V_D = -50$ V was not significant after 2000 mechanical bending cycles. On the other hand, it can be seen that μ_{sat} drastically decreases from 1.41 to 1.20 cm^2 V^{-1} s^{-1} after the first 50 bending cycles and gradually decreases to 0.92 cm^2 V^{-1} s^{-1} after 2000 bending cycles. Figure 8f shows the decrease in μ_{sat} as a function of bending cycles. A previous
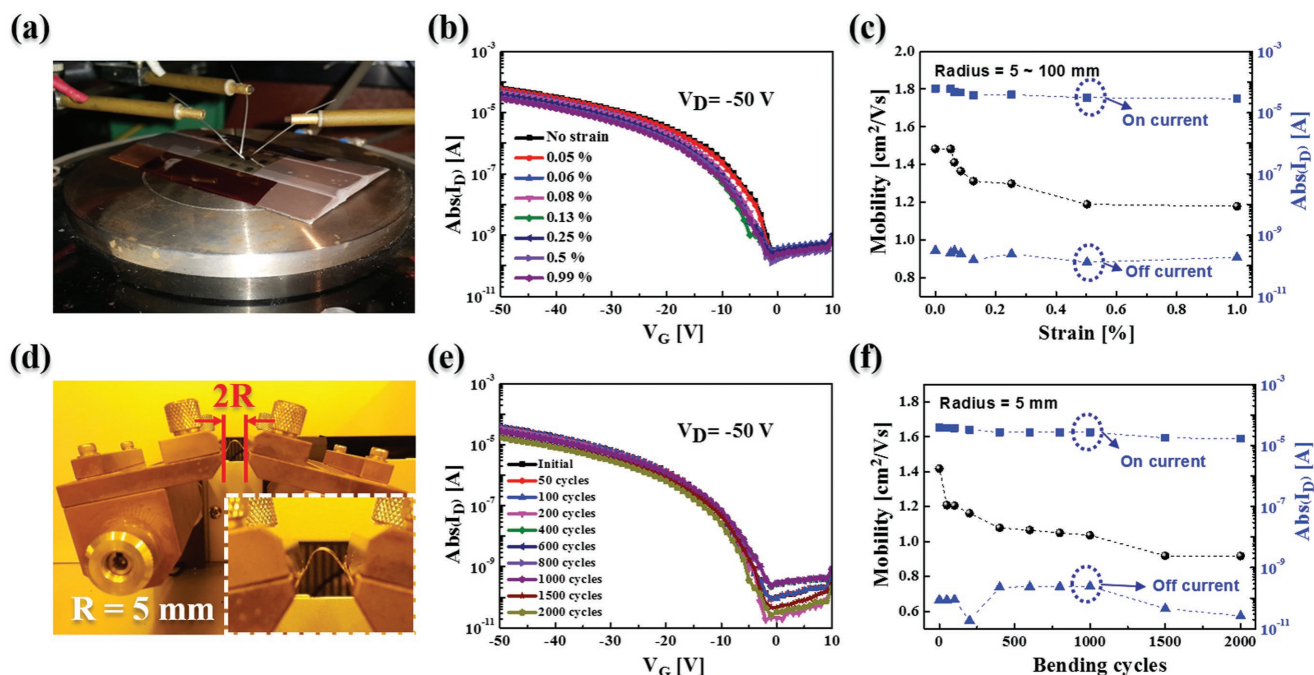
Figure 8. Digital camera image of flexible devices a) on the metal bending substrate and d) with the bending tester at $R = 5$ mm. The inset in (d) shows a zoomed-in optical image of the flexible OPT with the bending tester. Transfer characteristics at different b) tensile strains and e) bending cycles. Variation in μ_{sat}, on current and off current, as a function of c) applied tensile strain and f) bending cycles.

study showed that the decrease in mobility with the bending cycles is related to the phase transition in pentacene from a thin film phase to a bulk phase.[38] The observed mobility decrease after bending cycles can consequently be explained by the phase change because the bulk phase exhibits lower mobility than the thin-film phase. However, 2000 successive mechanical bending cycles confirm that the devices still exhibit a stable electrical property with the on/off ratio exceeding 10^5. Compared with the previously reported transistors that are based on pentacene as the semiconductor layer,
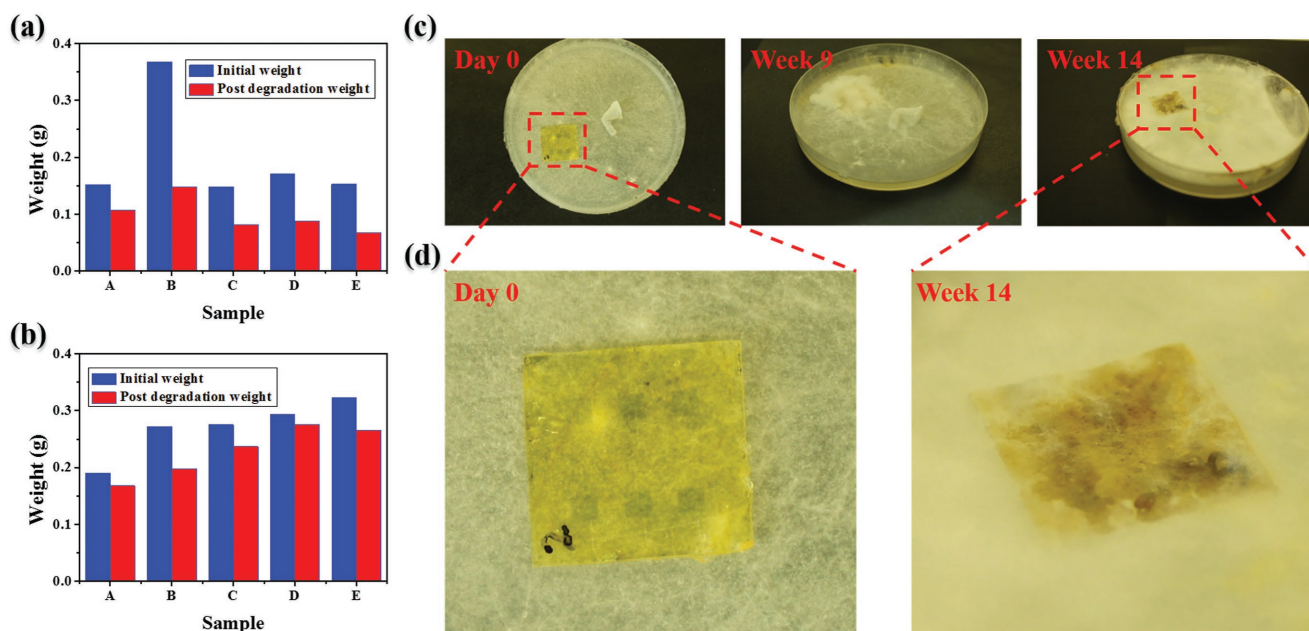

Figure 9. Fungal biodegradation tests of the OPTs with a) *P. placenta* and b) *P. chrysosporium*. Five samples were degraded at each test. c) A series of photographs observed on day 0 and weeks 9 and 14 after starting the degradation process with *P. placenta*. d) Magnified photographs of the OPTs taken at day 0 and after week 14 of degradation.

our device shows comparable mobility variation of 20% under bending with a radius of 5 mm and more stable operation with 65% of the original mobility after 2000 mechanical bending cycles.[24,38]

Finally, the fungal biodegradation test was performed, in order to prove the biodegradability of CNF substrate and the concept of the biodegradable electronics. **Figure 9** shows a sequence of fungal degradation tests on CNF-based OPT devices. Two wood decay fungi, brown rot fungus *Postia placenta* and white rot fungus *P. chrysosporium* were tested for the capacity of degradation on the nanofilm specimens. Figure 9a,b shows the weight loss result of OPTs on CNF substrates after *P. placenta* and *P. chrysosporium* for 14 weeks, respectively. Five replicas were made and degraded under the same conditions for each degradation test. Weight loss data have shown larger average degradation by *P. placenta* (47.22%, with a standard deviation (s.d.) of 11.85%) versus *P. chrysosporium* (15.4%, with a s.d. of 7.77%), suggesting *P. placenta* degrades the CNF films faster than *P. chrysosporium*. Figure 9c,d shows the images of the decaying process of the CNF substrate with OPT devices against *P. placenta*. Photos were taken at 0 day and after 9 and 14 weeks after starting the degradation test as presented in Figure 9c, showing that the fungi fully covered the sample after 9 weeks. *P. placenta* has shown heavy aggressive growth than *P. chrysosporium*, which is coincided with the weight loss data obtained in this study (Figure S5, Supporting Information).

The low dielectric constant of PMMA ($k = 3.5$) provides high leakage currents and limits the operating voltage. Some strategies, such as using a solvent with a large dipole moment, blending with a crosslinking agent, and using a bilayer structure with high-k dielectrics, can be used to lower the operating voltage of the devices with PMMA as the gate dielectric layer.[39,40] Regardless, the key demonstration here is the creation of flexible OPTs that are nontoxic, transparent, and biodegradable, as confirmed by the comprehensive characteristics.

3. Conclusions

In summary, we have demonstrated flexible, transparent organic phototransistors by using nontoxic pentacene active material and MoO_3-buffered IZO electrodes on a biodegradable CNF substrate. The transistor exhibits over 70% transmittance and excellent electrical characteristics with a saturation mobility of 1.40 cm^2 V^{-1} s^{-1}, showing good mechanical flexibility while maintaining stable operation under bending and after the bending cycles. The phototransistor can detect visible light and operates in photovoltaic (turned-on state at $V_G = -50$ V) and photocurrent (turn-off state, minimum I_D) modes under light illumination. The phototransistor also exhibits excellent biodegradation characteristics by decay fungi, showing that the combination of the environmentally nontoxic component as the active material and biodegradable substrate can be a way to make eco-friendly electronics. Overall, this demonstration suggests that biodegradable CNF films can be used as an alternative substrate for flexible electronics and that the phototransistors present the

considerable potential for the use in low-cost and eco-friendly disposable sensor systems.

4. Experimental Section

Thin-Film Transistor Fabrication: IZO as a gate electrode was sputtered with a radio-frequency magnetron system under fixed conditions (power = 150 W, Ar flow rate = 3.5 sccm, and deposition rate = 8 nm min^{-1}) on the CNF substrate at room temperature. A 500 nm thick PMMA (Sigma Aldrich; M_w = 120k, dielectric constant = 3.5) sheet was used as a dielectric material. The PMMA was dissolved in *n*-butyl acetate to obtain an 80 mg mL^{-1} concentration solution. The solution (preheated to 80 °C) was then spin-coated at 2000 rpm for 60 s, followed by thermal annealing at 100 °C for 30 min in the Ar-purged glove box. With a different metal shadow mask, a 70 nm thick pentacene as an organic semiconductor and a 20 nm thick MoO_3 as a buffer layer were deposited by thermal evaporation at a base pressure of $\approx 3 \times 10^{-6}$ torr with deposition rates of ≈ 1 and 0.49 Å s^{-1}, respectively. The bottom-gate/top-contact structure of the OPTs was completed with the formation of source/drain electrodes (IZO) by sputtering using a metal shadow mask at room temperature.

Electrical Characterization of OPTs: The electrical characteristics were measured using a Keithley-4200 semiconductor parameter analyzer in a dark box at room temperature. The fundamental device parameters, such as the saturation mobility (μ_{sat}) and threshold voltage (V_T), were extracted in the saturation regime with the gradual channel approximation equation. Transmittance and absorption were measured with a UV–visible spectroscope (Cary 5000, Varian). The topologies of the substrate, electrodes, dielectric, and semiconductor were characterized using AFM (XE-100, Park Systems Inc.). XRD analysis was performed using a Rigaku Smart Lab diffractometer operated at 45 kV and 200 mA using CuKα radiation. The photoresponse of the OPTs was characterized using a 150 W Xe arc lamp with filters for different light intensities (0.12, 0.36, 0.6, 0.84, and 1.2 mW cm^{-2}) and wavelengths (420 nm (blue), 550 nm (green), and 650 nm (red)). The surface states were analyzed using UPS (AXIS-NOVA, Kratos Inc.) with the incident UV light containing 21.22 eV photons (He I line). The bending tests were carried out with metal bending substrates ranging from 100 to 5 mm and a bending tester (z-tec, Inc.).

Fungal Biodegradation Test: To prepare for a fungal degradation test, isolates of two decay fungi, *P. placenta* (Fr.) M. Lars and Lomb. (MAD 698) and *P. chrysosporium* (ME 461), were grown and maintained on 22% malt extract agar (Difco, Detroit, MI) in Petri dishes (15 × 100 mm). Inoculum was incubated at 27 °C, 70% relative humidity (RH) room for 2 weeks. Nanofilm specimens were sized in a square shape (16 × 16 mm) and preconditioned at the incubator for 2 weeks. After weights were measured, specimens were laid on agar plates containing confluent fungal growth according to American Wood Preserver's Association E-10-06 Standard. Modifications were applied using Petri dishes to replace soil block culture bottles. No overlaying grids were used for Petri dish method. For degradation test, each fungal strain incorporated five identical specimens with one specimen per plate. Petri dishes were incubated at 27 °C, 70% RH to promote fungal growth over the specimens. Evaluations were observed on day 0 and weeks 9 and 14 and photography records were obtained at each time point.

Weight Loss Determination: Nanofilm specimens were harvest on week 14, brushed off fungal mycelia, and air dried for 48 hours and recondition at the incubator for 2 weeks to obtain final weights. Weight loss was determined by subtracting the reconditioned harvest weights from original conditioned weights. Percentage weight loss was also calculated.

Supporting Information

Supporting Information is available from the Wiley Online Library or from the author.

ADVANCED
SCIENCE NEWS
www.advancedsciencenews.com

ADVANCED
OPTICAL
MATERIALS
www.advopticalmat.de

Conflict of Interest

The authors declare no conflict of interest.

Keywords

biodegradation, flexible sensors, indium zinc oxide electrodes, organic phototransistors, thin-film transistors

[1] M. Irimia-Vladu, E. D. Glowacki, G. Voss, S. Bauer, N. S. Sariciftci, *Mater. Today* **2012**, *15*, 340.

[2] Q. Zhang, W. Z. Bao, A. Gong, T. Gong, D. K. Ma, J. Y. Wan, J. Q. Dai, J. N. Munday, J. H. He, L. B. Hu, D. H. Zhang, *Nanoscale* **2016**, *8*, 14237.

[3] H. L. Zhu, Z. Q. Fang, C. Preston, Y. Y. Li, L. B. Hu, *Energy Environ. Sci.* **2014**, *7*, 269.

[4] H. Y. Mi, C. H. Liu, T. H. Chang, J. H. Seo, H. L. Zhang, S. Cho, N. Behdad, Z. Q. Ma, C. H. Yao, Z. Y. Cai, S. Q. Gong, *Cellulose* **2016**, *23*, 1989.

[5] J. Huang, H. L. Zhu, Y. C. Chen, C. Preston, K. Rohrbach, J. Cumings, L. B. Hu, *ACS Nano* **2013**, *7*, 2106.

[6] H. L. Zhu, W. Luo, P. N. Ciesielski, Z. Q. Fang, J. Y. Zhu, G. Henriksson, M. E. Himmel, L. B. Hu, *Chem. Rev.* **2016**, *116*, 9305.

[7] Y. H. Jung, T. H. Chang, H. L. Zhang, C. H. Yao, Q. F. Zheng, V. W. Yang, H. Y. Mi, M. Kim, S. J. Cho, D. W. Park, H. Jiang, J. Lee, Y. J. Qiu, W. D. Zhou, Z. Y. Cai, S. Q. Gong, Z. Q. Ma, *Nat. Commun.* **2015**, *6*, 7170.

[8] J.-H. Seo, T.-H. Chang, J. Lee, R. Sabo, W. Zhou, Z. Cai, S. Gong, Z. Ma, *Appl. Phys. Lett.* **2015**, *106*, 262101.

[9] B. Lamprecht, R. Thunauer, M. Ostermann, G. Jakopic, G. Leising, *Phys. Status Solidi A* **2005**, *202*, R50.

[10] M. Anbia, N. Mohammadi, K. Mohammadi, *J. Hazard. Mater.* **2010**, *176*, 965.

[11] K. J. Baeg, M. Binda, D. Natali, M. Caironi, Y. Y. Noh, *Adv. Mater.* **2013**, *25*, 4267.

[12] R. Qiao, A. P. Roberts, A. S. Mount, S. J. Klaine, P. C. Ke, *Nano Lett.* **2007**, *7*, 614.

[13] S. W. Hwang, H. Tao, D. H. Kim, H. Y. Cheng, J. K. Song, E. Rill, M. A. Brenckle, B. Panilaitis, S. M. Won, Y. S. Kim, Y. M. Song, K. J. Yu, A. Ameen, R. Li, Y. W. Su, M. M. Yang, D. L. Kaplan, M. R. Zakin, M. J. Slepian, Y. G. Huang, F. G. Omenetto, J. A. Rogers, *Science* **2012**, *337*, 1640.

[14] C. Dagdeviren, S. W. Hwang, Y. W. Su, S. Kim, H. Y. Cheng, O. Gur, R. Haney, F. G. Omenetto, Y. G. Huang, J. A. Rogers, *Small* **2013**, *9*, 3398.

[15] S. W. Hwang, X. Huang, J. H. Seo, J. K. Song, S. Kim, S. Hage-Ali, H. J. Chung, H. Tao, F. G. Omenetto, Z. Q. Ma, J. A. Rogers, *Adv. Mater.* **2013**, *25*, 3526.

[16] D. W. Park, A. A. Schendel, S. Mikael, S. K. Brodnick, T. J. Richner, J. P. Ness, M. R. Hayat, F. Atry, S. T. Frye, R. Pashaie, S. Thongpang, Z. Q. Ma, J. C. Williams, *Nat. Commun.* **2014**, *5*, 5258.

[17] M. Choi, J. Choi, S. Kim, S. Nizamoglu, S. K. Hahn, S. H. Yun, *Nat. Photonics* **2013**, *7*, 987.

[18] E. Bystrenova, M. Jelitai, I. Tonazzini, A. N. Lazar, M. Huth, P. Stoliar, C. Dionigi, M. G. Cacace, B. Nickel, E. Madarasz, F. Biscarini, *Adv. Funct. Mater.* **2008**, *18*, 1751.

[19] M. Irimia-Vladu, *Chem. Soc. Rev.* **2014**, *43*, 6470.

[20] M. Kroger, S. Hamwi, J. Meyer, T. Riedl, W. Kowalsky, A. Kahn, *Appl. Phys. Lett.* **2009**, *95*, 123301.

[21] J. Meyer, S. Hamwi, M. Kroger, W. Kowalsky, T. Riedl, A. Kahn, *Adv. Mater.* **2012**, *24*, 5408.

[22] C. W. Chu, S. H. Li, C. W. Chen, V. Shrotriya, Y. Yang, *Appl. Phys. Lett.* **2005**, *87*, 193508.

[23] H. Klauk, *Chem. Soc. Rev.* **2010**, *39*, 2643.

[24] H. Yang, C. Yang, S. H. Kim, M. Jang, C. E. Park, *ACS Appl. Mater. Interfaces* **2010**, *2*, 391.

[25] T. S. Huang, Y. K. Su, P. C. Wang, *Appl. Phys. Lett.* **2007**, *91*, 092116.

[26] T. B. Singh, T. Meghdadi, S. Gunes, N. Marjanovic, G. Horowitz, P. Lang, S. Bauer, N. S. Sariciftci, *Adv. Mater.* **2005**, *17*, 2315.

[27] P. G. Schroeder, C. B. France, J. B. Park, B. A. Parkinson, *J. Appl. Phys.* **2002**, *91*, 3010.

[28] J. Puigdollers, C. Voz, A. Orpella, R. Quidant, I. Martin, M. Vetter, R. Alcubilla, *Org. Electron.* **2004**, *5*, 67.

[29] Y. J. Yun, C. Pearson, M. C. Petty, *J. Appl. Phys.* **2009**, *105*, 034508.

[30] B. Kang, M. Jang, Y. Chung, H. Kim, S. K. Kwak, J. H. Oh, K. Cho, *Nat. Commun.* **2014**, *5*, 4752.

[31] Y. L. Guo, G. Yu, Y. Q. Liu, *Adv. Mater.* **2010**, *22*, 4427.

[32] H. B. Zhang, X. J. Zhang, C. Liu, S. T. Lee, J. S. Jie, *ACS Nano* **2016**, *10*, 5113.

[33] Y. Y. Noh, D. Y. Kim, Y. Yoshida, K. Yase, B. J. Jung, E. Lim, H. K. Shim, *Appl. Phys. Lett.* **2005**, *86*, 043501.

[34] X. Liu, H. Zhao, G. Dong, L. Duan, D. Li, L. Wang, Y. Qiu, *ACS Appl. Mater. Interfaces* **2014**, *6*, 8337.

[35] F. Loffredo, A. Bruno, A. Mauro, I. A. Grimaldi, R. Miscioscia, G. Nenna, G. Pandolfi, M. Petrosino, F. Villani, C. Minarini, A. Facchetti, *Phys. Status Solidi A* **2014**, *211*, 460.

[36] J. H. Seo, K. Zhang, M. Kim, D. Zhao, H. Yang, W. Zhou, Z. Ma, *Adv. Opt. Mater.* **2016**, *4*, 120.

[37] J. H. Seo, T. Y. Oh, J. Park, W. D. Zhou, B. K. Ju, Z. Q. Ma, *Adv. Funct. Mater.* **2013**, *23*, 3398.

[38] Y. R. Su, J. L. Jiang, N. Ke, N. Zhao, W. G. Xie, J. B. Xu, *J. Mater. Chem. C* **2013**, *1*, 2585.

[39] R. P. Ortiz, A. Facchetti, T. J. Marks, *Chem. Rev.* **2010**, *110*, 205.

[40] N. B. Ukah, J. Granstrom, R. R. Sanganna Gari, G. M. King, S. Guha, *Appl. Phys. Lett.* **2011**, *99*, 243302.